

Journal Pre-proof

Synthesis of optically active chiral mesoporous molybdenum carbide film

Fusheng Zhang, Xintong Zheng, Cunli Wang, Dongdong Wang,
Xingya Xue, Guangyan Qing



PII: S1226-086X(20)30532-3
DOI: <https://doi.org/10.1016/j.jiec.2020.11.023>
Reference: JIEC 5304

To appear in: *Journal of Industrial and Engineering Chemistry*

Received Date: 30 September 2020
Revised Date: 25 November 2020
Accepted Date: 25 November 2020

Please cite this article as: Zhang F, Zheng X, Wang C, Wang D, Xue X, Qing G, Synthesis of optically active chiral mesoporous molybdenum carbide film, *Journal of Industrial and Engineering Chemistry* (2020), doi: <https://doi.org/10.1016/j.jiec.2020.11.023>

This is a PDF file of an article that has undergone enhancements after acceptance, such as the addition of a cover page and metadata, and formatting for readability, but it is not yet the definitive version of record. This version will undergo additional copyediting, typesetting and review before it is published in its final form, but we are providing this version to give early visibility of the article. Please note that, during the production process, errors may be discovered which could affect the content, and all legal disclaimers that apply to the journal pertain.

© 2020 Published by Elsevier.

Synthesis of optically active chiral mesoporous molybdenum carbide film

Fusheng Zhang,^{a,b} Xintong Zheng,^{a,c} Cunli Wang,^a Dongdong Wang,^a Xingya Xue,^a Guangyan Qing^{a,d*}

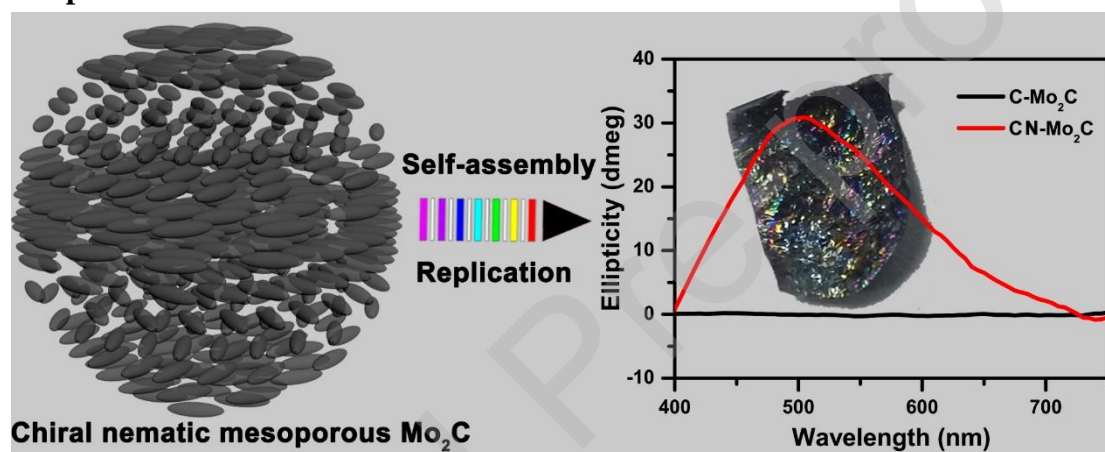
^aKey Laboratory of Separation Science for Analytical Chemistry, Dalian Institute of Chemical Physics, Chinese Academy of Sciences, Dalian, Liaoning, 116023, P. R. China

^bUniversity of Chinese Academy of Sciences, Beijing, 100049, P. R. China

^cPharmacy College, Dalian Medical University, Dalian, Liaoning, 116044, P. R. China

^dKey Laboratory of Advanced Energy Materials Chemistry (Ministry of Education), College of Chemistry, Nankai University, Tianjin, 300071, P. R. China

Graphical abstract



Abstract

A chiral nematic mesoporous molybdenum carbide film (CN-Mo₂C) was fabricated through the self-assembly of cellulose nanocrystal with peroxomolybdate. CN-Mo₂C exhibits a tunable chiral nematic structure by varying the ratio of constituents, enabling a surface area of 210 m² g⁻¹. Importantly, it shows a typical chiroptical feature through polarized optical microscopy and circular dichroism spectral analysis. As it has an excellent conductivity of 2.4×10^{-2} S cm⁻¹, we try to use CN-Mo₂C in the electrocatalytic HER production, presenting an efficient H₂ production capacity. It is a

versatile synthetic strategy that can conveniently enable other large-area macroscopic chiral metal-based materials.

Keyword: Chirality; Cellulose nanocrystal; Molybdenum; Structural tuning; Chiroptical property

Introduction

Chiral inorganic materials have attracted much attention because of their novel properties and wide applications in chiral plasmonics[1], chiroptical sensing[2], and asymmetric catalysis[3]. It is motivated by the self-evident significance of chirality for physics, chemistry, and biomedicine[4, 5]. Meanwhile, inorganic nanocrystals can be easily modulated through altering their size, shape, and ingredient, which is a promising platform for understanding the chiral origins. Research in this area points out the chiroptical activity can exist in inorganic substances, not exclusive preserve for the organism[6]. There are two available strategies for the synthesis of the chiral inorganic materials: (a) the co-assembly of chiral biological components (e.g., DNA, amino acids, and peptide) with metal precursors have achieved in the outstanding chiroptical activity of various chiral inorganic nanoparticles[7-10], and (b) sophisticated chiral ligands have been used to synthesize multifunctional pulverous chiral metal-organic frameworks[11] and perovskite nanocrystals[12, 13]. However, few successful examples have been demonstrated to enable these chiral systems to the advanced macroscopic robust chiral metal-based nanostructure. In contrast, large-area and easy-

to-prepare chiral inorganic film can have wide application prospects due to their operability in the application process.

Cellulose nanocrystal (CNC) is obtained by sulfuric acid-catalyzed hydrolysis of biomass and then hierarchically self-organize into the chiral nematic phase through electrostatic repulsion among sulfates[14]. A pioneer MacLachlan has reported many modes of co-assemble CNC with multiple precursors in aqueous solution to fabricate chiral nematic iridescent films. Because of the surface sulfate esters on CNCs, it is sensitive to the ionic strength. Varying the ionic strength in the assembly process is a powerful approach for controlling the reflected color of the iridescent film.[15] Color tuning is also possible for the pH values or precursor loading.[16] CNC as a bio-template can make the chiral nematic structure deliver into silica[17], carbon[18], titanium dioxide [19], cupric oxide[20], cobalt ferrite[21], and other metal-based matrixs[22, 23]. The pores of these long-range hierarchical materials are aligned in directional layers through a rotating stack. Thereupon, CNC-derived chiral nematic inorganic materials have been currently used for the development of novel sensors, catalyst supports, and energy storage materials[24-26]. However, the straightforward introduction of metallic ions or active metal alkoxides (such as $Zr(OC_4H_9)_4$) into the CNC system invariably disrupts the electrical balance of CNC and thus gelation in the mixture phase. So far, it is still a grand challenge to co-assemble CNC with metal precursors into the CNC-derived chiral metal-based materials.

Herein, we achieve that the peroxomolybdate (PM) solution self-assemble with CNC in an aqueous solution, forming a homogeneous mixture. After a series of ratio

optimization, the satisfactory resulting made the PM possible to retain the chiral nematic phase for the construction of Mo-based freestanding chiral nanostructured materials[27, 28]. Furthermore, this strategy can be realized in other peroxometallate compounds to fabricate chiral nematic inorganic nanostructure, including peroxotitanate, peroxovanadate, and peroxozirconate. As proof of concept, the incorporation of the PM solution into the CNC suspension fabricated a colorful PM/CNC composite film with the chiral nematic organization for the first time. Subsequent carbonization of the composite film and magnesiothermic reduction, a freestanding chiral nematic mesoporous molybdenum carbide film (CN-Mo₂C) was obtained in the final. Excitingly, the microstructural CN-Mo₂C in cross-section shows a layered structure with the helical axis of the chiral nematic phase. The signals of chiroptical activity in iridescent CN-Mo₂C was recorded through polarized optical microscopy (POM) and circular dichroism (CD) spectra. Briefly, a large-area chiral nematic origination of structural replication in Mo₂C film was attributed to the transference of the chiral nematic phase of CNC. Given that molybdenum carbide is a kind of practical and promising future catalysts in the hydrogen evolution reaction (HER) [29, 30]. We try to use the CN-Mo₂C in the electrocatalytic HER production and it enabled a boost of the electrocatalytic activity compared with disordered commercial molybdenum carbide (C-Mo₂C). This attempt is anticipated to offer a “one-pot” versatile strategy to fabricate chiral inorganic materials and optimize catalytic performance, and therefore an advantage in the asymmetric chemistry or energy conversion field.

Experimental section

Materials and Characterization. All reagents and solvents without further purification including molybdenum powder (99.5%), ammonium molybdate (99%), molybdenum carbide (99.9%), hydrogen peroxide (H₂O₂, 30%) through standard suppliers. Polystyrene Petri dishes with a diameter of 50 cm were supplied by Guangzhou Jet Bio-Filtration Co., Ltd. Suspension of cellulose nanocrystal (CNC) was prepared from acid-catalyzed hydrolysis of degreasing cotton in a procedure described previously,[31] except that the suspension was concentrated in a rotary evaporator to 4.0 wt%. The functionalization with –OSO₃– groups on CNC was evaluated by conductometric titration with 0.92 wt% S content (Fig. S2a) [32]. Zeta potential was recorded through a Zetasizer ZS90 from Malvern Instruments. Conductometric measurement was measured on a conductivity meter with DDS-11A. UV–visible spectroscopy was recorded through a PerkinElmer Lambda 365, and circular dichroism (CD) was performed using a BioTools MOS450 spectropolarimeter. Polarized optical microscopy (POM) images were performed on a Leica DM4P microscope. Infrared (IR) spectra were collected on a Nicolet iS50 spectrometer (America). Scanning electron microscope (SEM) images were collected using a Carl Zeiss Helium ion microscope. Brunauer–Emmet–Teller (BET) adsorption isotherm curve was measured on a QuantaChrome nitrogen adsorption/desorption apparatus with QUADRASORB SI. Transmission electron microscope (TEM) images were collected on a JEOL JEM-2100 at an accelerating voltage of 200 kV with a LaB6 filament. Powder X-ray diffraction (XRD) patterns were obtained on a PANalytical X'pert Pro-1 at 5–80 ° with 6 ° min⁻¹.

Thermogravimetric analysis (TGA) was measured using a Diamond TG/DTA Instrument (STA 449 F3, Netzsch, Germany) up to 800°C with a heating rate of 10.0°C min⁻¹. Electrical conductivity was measured by using the standard four-probe method with at least three measurements.

Preparation of PM/CNC composite film (MCF). Molybdenum powder (5 g) was slowly added into H₂O₂ (45 mL) at ice-bath under quickly stirring until obtaining a clear and transparent yellow solution. The obtained mixture was continued with stirring overnight for decomposing residual H₂O₂ and then peroxomolybdate (PM) was obtained after diluting the above mixture into 2 wt% solutions. Fig. S2b indicates the stability of PM through a powder X-ray diffraction pattern. To prepare PM/CNC composite film, 4 mL of CNC suspension after sonication for 10 min were firstly mixed with 2.0 mL of PM and stirred at room temperature for 1 h access to a homogeneous mixture. Briefly, the mixture was transferred into polystyrene Petri dishes (5 cm) to organize into a chiral nematic phase. During slow solvent evaporation for 48 h, the formation of iridescent yellow PM/CNC composite film with chiral nematic structure. Additional samples were prepared by using an identical procedure except for varying the amount of PM.

Preparation of chiral nematic mesoporous molybdenum carbide film. The as-prepared MCF-2.0 was first carbonized by heating the sample under flowing nitrogen to 600°C for 6 h to generate MoO₃/C composites. The black MoO₃/C materials (80 mg) and Mg turnings (400 mg) were placed at a ceramic reaction boat and annealed under flowing nitrogen to 650°C at a rate of 2°C min⁻¹ and held at this temperature for 12 h.

Excess Mg was used to ensure the complete reduction of MoO₃. The resulting Mo₂C/C composites after magnesiothermic reduction were then calcined at 400°C in air for 1 h to eliminate residual carbon, giving chiral nematic mesoporous Mo₂C films before Mo₂C/C were treated with 0.5 M HCl at room temperature for 2 h to dissolve the MgO byproduct.

Electrochemical experiments. All the electrochemical experiments were conducted on an electrochemical workstation (CHI 760e). For the HER of two catalysts, a three-electrode cell was operated in 0.50 M H₂SO₄. Typically, 3 mg of catalyst and 80 mL of 5 wt% Nafion solution were dispersed in 1 mL of a solution of deionized water and ethanol (4:1 in volume ratio) [33]. After sonication for 30 min, 5 μ L catalyst slurry was dropped onto smooth glassy carbon electrodes with a diameter of 3 mm and dried in an oven of 30°C. The mass loading was about 0.213 mg cm⁻². Carbon rod and Ag/AgCl (in 1.0 M KCl) were used as the counter and reference electrodes, respectively. The linear sweep voltammograms were collected in an H₂-purged cell at a scan rate of 5 mV s⁻¹. To estimate the electroactive surface area of Mo₂C, cyclic voltammograms were measured between 0.10 – 0.30 V vs. SHE with scan rates of 20, 50, 75, 100, 150, and 200 mV s⁻¹. Electrochemical impedance (EIS) measurements were carried out from 100 kHz to 0.1 Hz with an amplitude of 10 mV at selected values of overpotentials. The potential was converted to SHE via the equation: $E_{\text{SHE}} = E_{\text{Ag/AgCl}} + 0.059\text{pH} + E^{\circ}_{\text{Ag/AgCl}}$.

Results and discussion

A typical preparation of freestanding PM/CNC composite film is illustrated in Scheme 1. CNC suspension (4 wt%, pH =2.6) was mixed with a volume of yellow PM

(2 wt%, pH=1.9), subsequently obtaining a homogeneous PM/CNC mixture (Fig. S1a). Some small tactoids are observed through POM after the water evaporated for 12 hours (Fig. S1b). Then totally drying under ambient temperature, iridescent PM/CNC composite films were obtained (Fig. 1a). Thermogravimetric analysis (TGA, Fig. S2c) reveals the thermal decomposition of PM between 50 and 250°C, and PM has an overall mass loss of ~80 wt%. Infrared spectra (IR, Fig. S2d) of the PM solid shows a series of characteristic peaks, such as O–H at ~3640 cm⁻¹, O–H at ~1620 cm⁻¹[34], Mo=O at ~980 and 940 cm⁻¹, and Mo–O at ~630 cm⁻¹[35, 36]. These features indicate that PM can form a stable self-assembled structure in the CNC aqueous solution.

Our approach to regulating the chiral nematic structure of PM/CNC films (MCFs) was operated by the modulation of PM loadings with a range of 1.0, 1.5, 2.0, and 2.5 mL. Fig. 1a shows three iridescent MCFs (i.e., MCF-1.0, MCF-1.5, and MCF-2.0 with a diameter of 5 cm), changing from blue, green to yellow in appearance. This color variation was recorded by UV-Vis spectroscopy (Fig. 1b upper panel), displaying as an obvious red-shift in transmission peaks. This color-changing was also observed in their POM images (Fig. 1c), along with a strong birefringence characteristic of chiral nematic ordering. CD spectra (Fig. 1b lower panel) show intense signal peaks with intensity greater than 2,000 millidegrees for all of the MCFs. This confirmation indicates the left-handed chiral nematic structure of these films. Besides, their CD shows a similar peak shift with that of the UV-vis. To the best of our knowledge, no attempt has yet been made to prepare the Mo-based composite films of intensely optical activity. These pieces of evidence demonstrate the MCF composite films can be endowed with the

chiral nematic phase of CNC and the tunable chiral nematic structure was available through controlling the amount of PM. However, when the 2.5 mL volume of PM was added into CNC suspension, the casting MCF-2.5 (Fig. S3a) shows the weak character of the chiral nematic phase as confirmed by POM (Fig. S3b) and SEM (Fig. S3c).

Confirmed by the above investigation, these MCF composites show the tunability of the chiral nematic structure. This tunability can be explained by the following de Vries equation:[37] $\lambda_{max} = n_{avg} \cdot P$, where λ_{max} is the reflected wavelength at normal incident light. n_{avg} and P are the average refractive index and helical pitch of the material, respectively. The reflected wavelength from MCF-1.0, MCF-1.5, to MCF-2.0 shows a red-shifted reflectance as recorded through UV-Vis spectra (Fig. 1b), which could explain through the increase of n_{avg} or P in these films. SEM recorded their actual P values that correspond to successive bilayer distances. The cross-sectional SEM images of these films show similar periodic layered structures but different in the increase of interlayer distances (Fig. 1d, 286, 381, and 550 nm). Furthermore, there is another attention in the SEM images of MCF-2.0 that rod-like morphology of obvious twisting in a counter-clockwise direction presents the left-handed chiral nematic structure. The resulting is consistent with the positive absorption band in CD. These investigations provide solid evidence that a self-assembly route to MCF is available, and their chiral structure easily realizes modulation through a ratio control of PM loading into the CNC system.

As proof of concept, CNC bio-templates can be used to make the large-area chiral molybdenum-based film. A versatile MCF-2.0 was firstly pyrolyzed under N_2 at $600^\circ C$,

giving a bulk glossy black MoO₃/C film (Fig. 2a). The cross-sectional SEM images of MoO₃/C film (Figs. 2b, c) show a similar successive layer to MCF-2.0 in Fig. 1d, except that the bilayer distance of MoO₃/C film is narrower. The conversion process of MCF-2.0 into MoO₃/C film was determined by TGA (Fig. 2d) and PXRD (Fig. 2e). The TGA curve of MCF-2.0 shows an approximate 35 % yield of carbon in MoO₃/C composite. MoO₃/C presents excellent thermal stability due to the formation of crystalline structures. The structural composition was confirmed by XRD patterns. MCF-2.0 shows two broad characteristic peaks of the CNC crystalline at $2\theta \approx 16^\circ$ and 24° . After carbon conversion, MoO₃/C shows the disappeared characteristic peaks of CNC, and three new peaks appeared at $2\theta \approx 26^\circ$, 37° , and 52° that belonged to MoO₃ crystals [17, 38, 39]. These investigations confirm that the chiral nematic order of the CNC is reserved and the carbonization reaction converted the PM to MoO₃.

To prepare the porous Mo₂C film, the above MoO₃/C film was treated through magnesiothermic reduction, producing a colorful hybrid film (Fig. S4). Then, the treatment of the hybrid with an aqueous HCl solution removed residual MgO. Finally, an iridescent molybdenum carbide film (CN-Mo₂C, Fig. 3a) was obtained. CN-Mo₂C shows the strong birefringence in the POM image (Fig. 3b and Video S1). CN-Mo₂C presents a β -phase, which PXRD pattern (Fig. 3e) demonstrates three typical characteristic peaks of (002), (110), and (101) [33]. It is recognized that the unique property of chiral nanostructure is the optical activity, in which this property is associated with the circular dichroism phenomenon [40, 41]. CD spectra of the CN-Mo₂C (Fig. 3f) show a broadband polarization absorption, while the C-Mo₂C (black

line in Fig. 2f) did not display any optical activity. To our knowledge, this is the first report about CNC self-assembly of Mo₂C materials with the tunable chiroptical property. The chiral activity of CN-Mo₂C is obtained from the chirality transfer of CNC, constructing chiral nematic morphologies via bottom-up self-organization. Research in this area breaks the morphological barrier between the abiotic and the biotic, providing a powerful platform for exploring chiroptical potentials in the multifunctional inorganic material[6, 42]. The g_{abs} is the absorptive dissymmetry factor of chiral materials. Some reports have measured that g_{abs} values in thin hybrid films are typically in the range of 10^{-4} – 10^{-2} [43-45]. Experimentally, the equation for calculating the g_{abs} value in a model is given below: $g_{\text{abs}} = \text{CD}(\text{mdeg})/(32980 \cdot \text{Abs})$. The absorbance of CN-Mo₂C was recorded through UV-Vis spectra as the following Fig. S5. According to the equation, CN-Mo₂C shows the g_{abs} value of 0.008 at the wavelength of approximately 500 nm.

The CNC of liquid crystal ordering is a promising template as previously reported for a chiral nematic mesoporous silica[17]. CN-Mo₂C has the chiral nematic structure with a long-range order of successive layers in the entire film through SEM (Fig. 3d). This investigation reveals that CN-Mo₂C preserved the structural integrity of the chiral nematic order even though the treatment of magnesiothermic reduction. Meanwhile, the perpendicular surface of CN-Mo₂C through SEM (Fig. 3c and Figs. S6a, b) shows randomly distributed vertical nanosheets. Transmission electron microscopy (TEM) of the CN-Mo₂C shows rodlike porous at the microscopic scale (Fig. S7). The porous structure of CN-Mo₂C was analyzed by nitrogen adsorption/desorption (Fig. 3g), which is a surface area of 210 m² g⁻¹ and an average pore size of 3 nm. These results confirm

that the chiral nematic structure of CNC is embedded in the mesoporous Mo₂C, and this strategy can be used in other metal-based materials.

An important application for porous Mo₂C is in electrocatalytic HER production, which shows an excellent conductivity of $2.4 \times 10^{-2} \text{ S cm}^{-1}$ at 25°C. We evaluated the electrocatalytic activity of CN-Mo₂C and C-Mo₂C for HER by linear sweep voltammetry (LSV) in 0.50 M H₂SO₄[46, 47]. Fig. 4a shows the polarization curves with a scan rate of 5 mV s^{-1} . In this experiment, each catalyst with an approximately loading amount of $0.213 \text{ mg}\cdot\text{cm}^{-2}$ was coated on glassy carbon. Furthermore, we used the Tafel slope to study the intrinsic activity of catalysts of hydrogen evolution, in which a smaller Tafel slope represents a faster HER efficiency[48]. According to the Tafel equation: $\eta = b \log(j) + a$, where η is the overpotential, b , j , and a are the Tafel slope, current density, and constant, respectively. Tafel analysis (Fig. 4b) gave two slopes of 88 and $148 \text{ mV}\cdot\text{dec}^{-1}$ with relevant to CN-Mo₂C and C-Mo₂C, respectively. Molybdenum has attracted numerous research interests due to its Pt-like electronic structure. As a result, a series of sophisticated and extraordinary molybdenum-based catalysts have emerged, including molybdenum phosphide[49], MoNi₄[50], and molybdenum disulfide[51]. Compared with these reported systems, this CN-Mo₂C not only has a large-area and low-cost economy but also shows a well-recognized electrocatalytic activity. Evidentially, the chiral nematic nanostructure of CN-Mo₂C contributed to a higher exposed surface area, leading to higher specific current density and a smaller Tafel slope. The electroactive surface area of a catalyst is a critical factor for evaluating HER. Cyclic voltammetry (CV, Fig. 4c) of CN-Mo₂C was performed

continuously in 0.5 M H₂SO₄ and recorded between 0.10 and 0.30 V versus reversible hydrogen electrode (RHE). The CV of CN-Mo₂C shows a rectangular shape with no noticeable redox peaks, indicating a stable charging–discharging process at different scan rates. Electrochemical impedance spectroscopy is another important criterion for studying the transport kinetics of electrocatalyst. Fig. 4d shows the Nyquist plot of CN-Mo₂C and C-Mo₂C are 57 Ω and 368 Ω at $\eta = -400$ mV, respectively. It can be seen that CN-Mo₂C has one smaller depressed semicircle in the high-frequency region resulting from its small charge transfer resistance. Demonstrating that the large BET surface area likely facilitated the high HER activity[52].

Conclusions

In summary, chiral nematic mesoporous Mo₂C films were first synthesized through the self-assembly of CNC with water-soluble PM. The Mo₂C film shows remarkable chiroptical properties and ordered helical layers via CD and SEM characteristics. This strategy can be extended to develop novel chiral Mo-based or Mo-derived materials with desirable functionalities. Following this study, numerous multi-type chiral inorganic materials (V₂C, TiC, or V-Mo binary hybrid) with a broadband chiroptical activity can be created.

Declaration of interests

The authors declare that they have no known competing financial interests or personal relationships that could have appeared to influence the work reported in this paper.

Acknowledgements

This work was supported by the National Natural Science Foundation of China

(21775116 and 21922411), LiaoNing Revitalization Talents Program (XLYC1802109) and DICP Innovation Funding (DICP-RC201801).

References

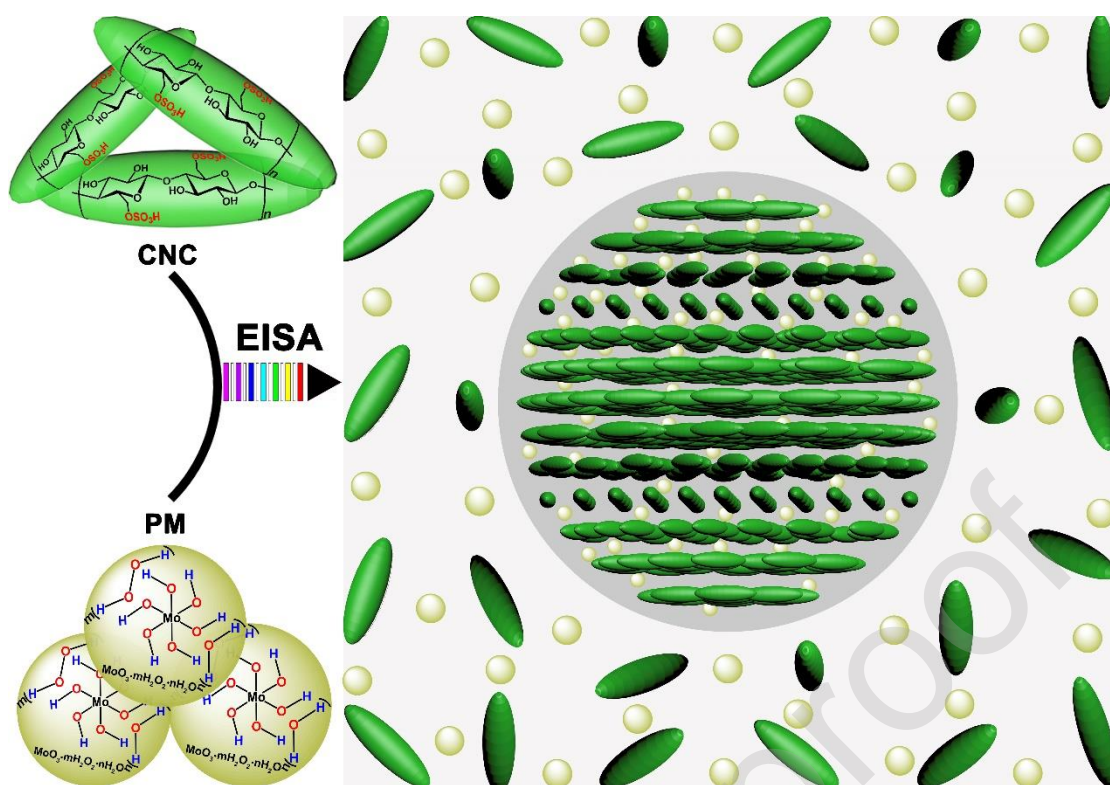
- [1] Z. Cheng, Y. Ma, L. Yang, F. Cheng, Z. Huang, A. Natan, H. Li, Y. Chen, D. Cao, Z. Huang, Y. Wang, Y. Liu, R. Yang, H. Zhu, *Adv. Opt. Mater.* 0 (2019) 1801816.
- [2] L. Xu, M. Sun, P. Cheng, R. Gao, H. Wang, W. Ma, X. Shi, C. Xu, H. Kuang, *Adv. Funct. Mater.* 28 (2018) 1707237.
- [3] T. Yutthalekha, C. Wattanakit, V. Lapeyre, S. Nokbin, C. Warakulwit, J. Limtrakul, A. Kuhn, *Nat. Commun.* 7 (2016) 12678.
- [4] Y. Xia, Y. Zhou, Z. Tang, *Nanoscale* 3 (2011) 1374.
- [5] W. Ma, L. Xu, A.F. de Moura, X. Wu, H. Kuang, C. Xu, N.A. Kotov, *Chem. Rev.* 117 (2017) 8041-8093.
- [6] Y. Li, X. Wang, J. Miao, J. Li, X. Zhu, R. Chen, Z. Tang, R. Pan, T. He, J. Cheng, *Adv. Mater.* 32 (2020) 1905585.
- [7] S. Che, Z. Liu, T. Ohsuna, K. Sakamoto, O. Terasaki, T. Tatsumi, *Nature* 429 (2004) 281-284.
- [8] H.E. Lee, H.Y. Ahn, J. Mun, Y.Y. Lee, M. Kim, N.H. Cho, K. Chang, W.S. Kim, J. Rho, K.T. Nam, *Nature* 556 (2018) 360-365.
- [9] Q. Jiang, X. Xu, P.-A. Yin, K. Ma, Y. Zhen, P. Duan, Q. Peng, W.-Q. Chen, B. Ding, *J. Am. Chem. Soc.* 141 (2019) 9490-9494.
- [10] W. Jiang, Z.-b. Qu, P. Kumar, D. Vecchio, Y. Wang, Y. Ma, J.H. Bahng, K. Bernardino, W.R. Gomes, F.M. Colombari, A. Lozada-Blanco, M. Veksler, E. Marino,

- A. Simon, C. Murray, S.R. Muniz, A.F. de Moura, N.A. Kotov, *Science* (2020) eaaz7949.
- [11] T. Kitao, Y. Nagasaka, M. Karasawa, T. Eguchi, N. Kimizuka, K. Ishii, T. Yamada, T. Uemura, *J. Am. Chem. Soc.* 141 (2019) 19565-19569.
- [12] T. He, J. Li, X. Li, C. Ren, Y. Luo, F. Zhao, R. Chen, X. Lin, J. Zhang, *Appl. Phys. Lett.* 111 (2017) 151102.
- [13] J. Ma, C. Fang, C. Chen, L. Jin, J. Wang, S. Wang, J. Tang, D. Li, *ACS Nano* 13 (2019) 3659-3665.
- [14] R.H. Marchessault, F.F. Morehead, N.M. Walter, *Nature* 184 (1959) 632-633.
- [15] X.M. Dong, T. Kimura, J.-F. Revol, D.G. Gray, *Langmuir* 12 (1996) 2076-2082.
- [16] M. Giese, L.K. Blusch, M.K. Khan, M.J. MacLachlan, *Angew. Chem. Int. Ed.* 54 (2015) 2888-2910.
- [17] K.E. Shopsowitz, H. Qi, W.Y. Hamad, M.J. MacLachlan, *Nature* 468 (2010) 422-425.
- [18] K.E. Shopsowitz, W.Y. Hamad, M.J. MacLachlan, *Angew. Chem. Int. Ed.* 123 (2011) 11183-11187.
- [19] T.-D. Nguyen, J. Li, E. Lizundia, M. Niederberger, W.Y. Hamad, M.J. MacLachlan, *Adv. Funct. Mater.* 0 (2019) 1904639.
- [20] C.M. Walters, K.R. Adair, W.Y. Hamad, M.J. MacLachlan, *Eur. J. Inorg. Chem.* 2020 (2020) 3937-3943.
- [21] N. Thi Thanh Dang, T.-D. Nguyen, E. Lizundia, T. Quoc Le, M.J. MacLachlan, *ChemistrySelect* 5 (2020) 8207-8217.

- [22] K.R. Phillips, T. Shirman, E. Shirman, A.V. Shneidman, T.M. Kay, J. Aizenberg, *Adv. Mater.* 30 (2018) 1706329.
- [23] A. Ivanova, B. Frka-Petesic, A. Paul, T. Wagner, A.N. Jumabekov, Y. Vilk, J. Weber, J. Schmedt auf der Günne, S. Vignolini, M. Tiemann, D. Fattakhova-Rohlfing, T. Bein, *ACS Appl. Mater. Interfaces* 12 (2020) 12639-12647.
- [24] T. Hiratani, O. Kose, W.Y. Hamad, M.J. MacLachlan, *Mater. Horiz.* 5 (2018) 1076-1081.
- [25] R.M. Parker, G. Guidetti, C.A. Williams, T. Zhao, A. Narkevicius, S. Vignolini, B. Frka-Petesic, *Adv. Mater.* 30 (2018) 1704477.
- [26] W. Chen, H. Yu, S.-Y. Lee, T. Wei, J. Li, Z. Fan, *Chem. Soc. Rev.* 47 (2018) 2837-2872.
- [27] M.H. Dickman, M.T. Pope, *Chem. Rev.* 94 (1994) 569-584.
- [28] L. Zong, C. Wang, A.M.P. Moeljadi, X. Ye, R. Ganguly, Y. Li, H. Hirao, C.-H. Tan, *Nat. Commun.* 7 (2016) 13455.
- [29] L. Liao, S. Wang, J. Xiao, X. Bian, Y. Zhang, M.D. Scanlon, X. Hu, Y. Tang, B. Liu, H.H. Girault, *Energy Environ. Sci.* 7 (2014) 387-392.
- [30] T. Ouyang, A.-N. Chen, Z.-Z. He, Z.-Q. Liu, Y. Tong, *Chem. Commun.* 54 (2018) 9901-9904.
- [31] F. Zhang, D. Wang, H. Qin, L. Feng, X. Liang, G. Qing, *ACS Appl. Mater. Interfaces* 11 (2019) 13114-13122.
- [32] T. Abitbol, E. Kloser, D.G. Gray, *Cellulose* 20 (2013) 785-794.
- [33] C. Tang, A. Sun, Y. Xu, Z. Wu, D. Wang, *J. Power Sources* 296 (2015) 18-22.

- [34] T.-D. Nguyen, E. Lizundia, M. Niederberger, W.Y. Hamad, M.J. MacLachlan, *Chem. Mater.* 31 (2019) 2174-2181.
- [35] Y. Liu, S. Yang, Y. Lu, N.y.V. Podval'naya, W. Chen, G.S. Zakharova, *Appl. Surf. Sci.* 359 (2015) 114-119.
- [36] A. Chithambararaj, N.S. Sanjini, A.C. Bose, S. Velmathi, *Catal. Sci. Technol.* 3 (2013) 1405-1414.
- [37] H.d. Vries, *Acta Crystallogr.* 4 (1951) 219-226.
- [38] J.Z. Ou, J.L. Campbell, D. Yao, W. Wlodarski, K. Kalantar-zadeh, *J. Phys. Chem. C* 115 (2011) 10757-10763.
- [39] B.Y. Zhang, A. Zavabeti, A.F. Chrimes, F. Haque, L.A. O'Dell, H. Khan, N. Syed, R. Datta, Y. Wang, A.S.R. Chesman, T. Daeneke, K. Kalantar-zadeh, J.Z. Ou, *Adv. Funct. Mater.* 28 (2018) 1706006.
- [40] H.-Y. Wong, W.-S. Lo, K.-H. Yim, G.-L. Law, *Chem* 5 (2019) 3058-3095.
- [41] A. Kuzyk, R. Schreiber, Z. Fan, G. Pardatscher, E.-M. Roller, A. Högele, F.C. Simmel, A.O. Govorov, T. Liedl, *Nature* 483 (2012) 311.
- [42] H. Kuang, C. Xu, Z. Tang, *Adv. Mater.* 32 (2020) 2005110.
- [43] B.A. San Jose, S. Matsushita, K. Akagi, *J. Am. Chem. Soc.* 134 (2012) 19795-19807.
- [44] C.-J. Kim, A. Sánchez-Castillo, Z. Ziegler, Y. Ogawa, C. Noguez, J. Park, *Nat. Nanotechnol.* 11 (2016) 520-524.
- [45] J.-R. Jiménez, B. Doistau, C.M. Cruz, C. Besnard, J.M. Cuerva, A.G. Campaña, C. Piguet, *J. Am. Chem. Soc.* 141 (2019) 13244-13252.

- [46] H.B. Wu, B.Y. Xia, L. Yu, X.-Y. Yu, X.W. Lou, Nat. Commun. 6 (2015) 6512.
- [47] H. Zhang, Z. Ma, G. Liu, L. Shi, J. Tang, H. Pang, K. Wu, T. Takei, J. Zhang, Y. Yamauchi, J. Ye, Npg Asia Mater. 8 (2016) e293.
- [48] H. Wang, X. Xu, B. Ni, H. Li, W. Bian, X. Wang, Nanoscale 9 (2017) 15895-15900.
- [49] X. Chen, D. Wang, Z. Wang, P. Zhou, Z. Wu, F. Jiang, Chem. Commun. 50 (2014) 11683-11685.
- [50] J. Zhang, T. Wang, P. Liu, Z. Liao, S. Liu, X. Zhuang, M. Chen, E. Zschech, X. Feng, Nat. Commun. 8 (2017) 15437.
- [51] J. Benson, M. Li, S. Wang, P. Wang, P. Papakonstantinou, ACS Appl. Mater. Interfaces 7 (2015) 14113-14122.
- [52] G. Humagain, K. MacDougall, J. MacInnis, J.M. Lowe, R.H. Coridan, S. MacQuarrie, M. Dasog, Adv. Energy. Mater. 8 (2018) 1801461.



Scheme 1. Schematic illustrating of PM/CNC films with a chiral nematic structure owing to the self-ordering of CNC templates.

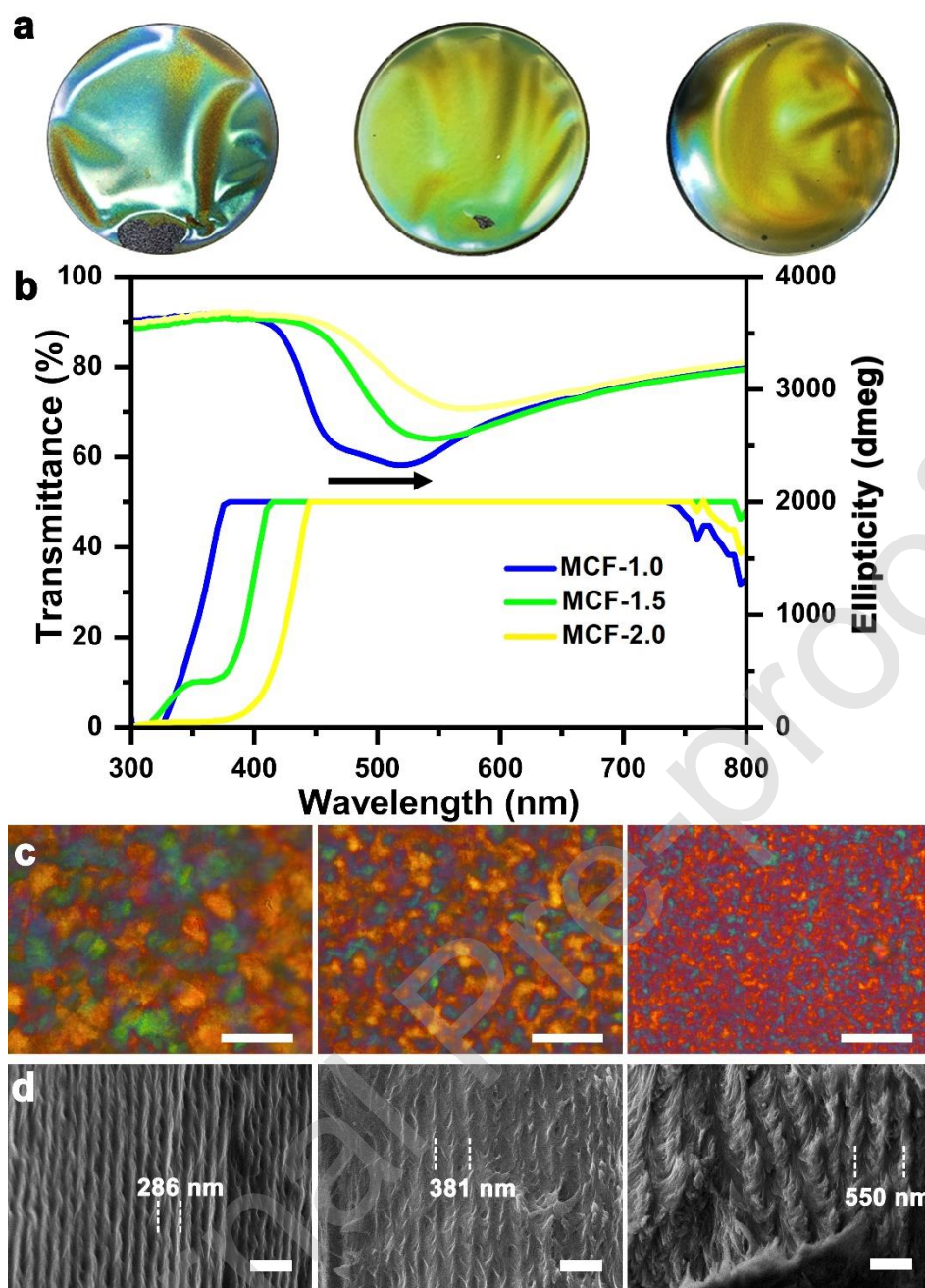


Fig. 1. Characterization data of three PM/CNC composite films. (a) Photographs of these films, from left to right: MCF-1.0, MCF-1.5, and MCF-2.0 (diameter, 5 cm) showing different structural colours under white light illumination. (b) UV-vis transmission spectra and positive CD spectra of PM/CNC films with the increasing amounts of PM loading showing a red-shift wavelength. (c) POM images of the above PM/CNC films taken with crossed polarizers (scale bar, 50 μm). (d) Cross-sectional SEM images for these PM/CNC films showing the helical pitch distance (scale bar, 500 nm).

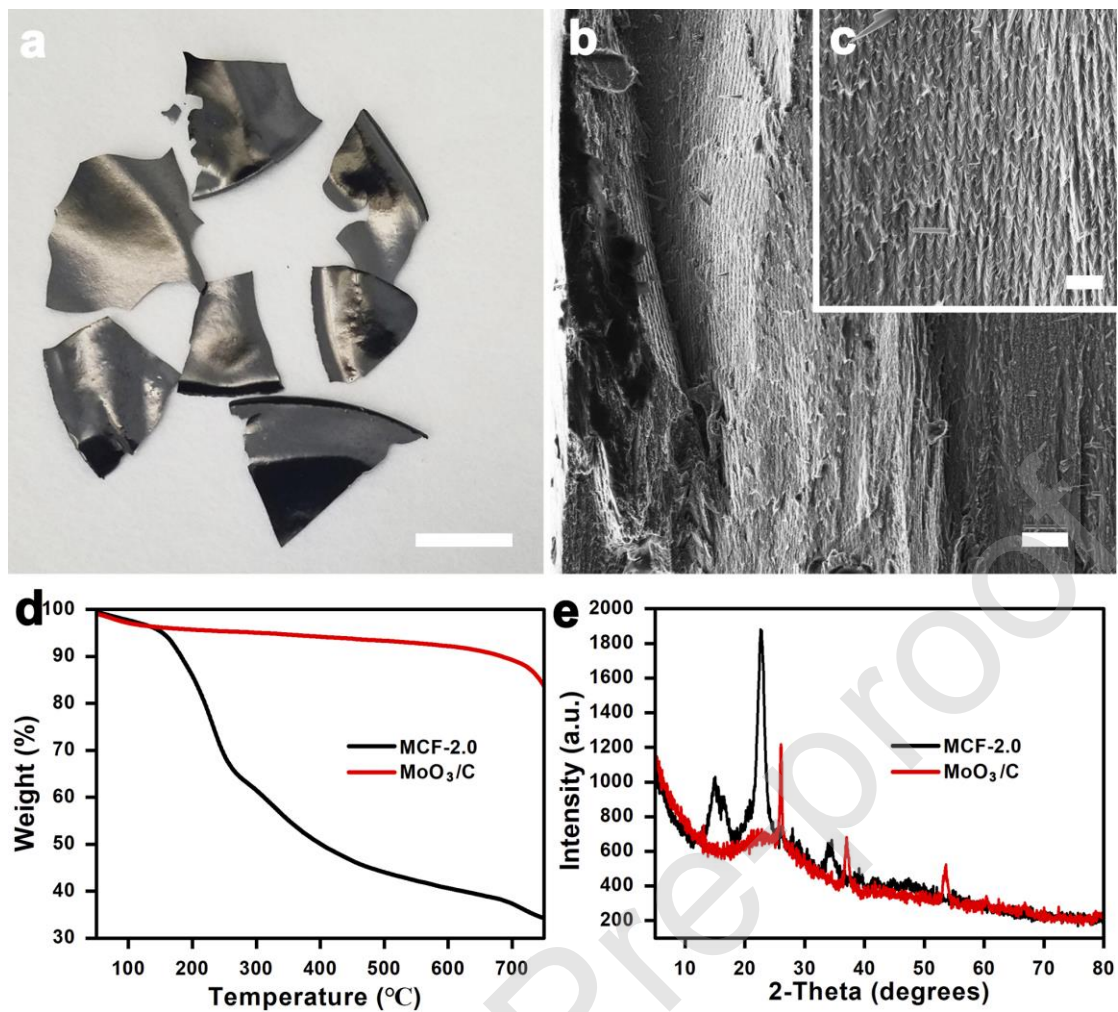


Fig. 2. Conversion of MCF-2.0 into MoO₃/C film. (a) Photos of MoO₃/C films with a bulk glossy black appearance (scale bar, 1 cm). (b) SEM images of fracture cross-section of MoO₃/C film shows the stacked layers of the chiral nematic phase (scale bar, 2 μ m). (c) Higher magnification reveals the helical pitch distance (scale bar, 500 nm). TGA curves (d) and PXRD patterns (e) of the MoO₃/C composites after the carbonization of MCF-2.0.

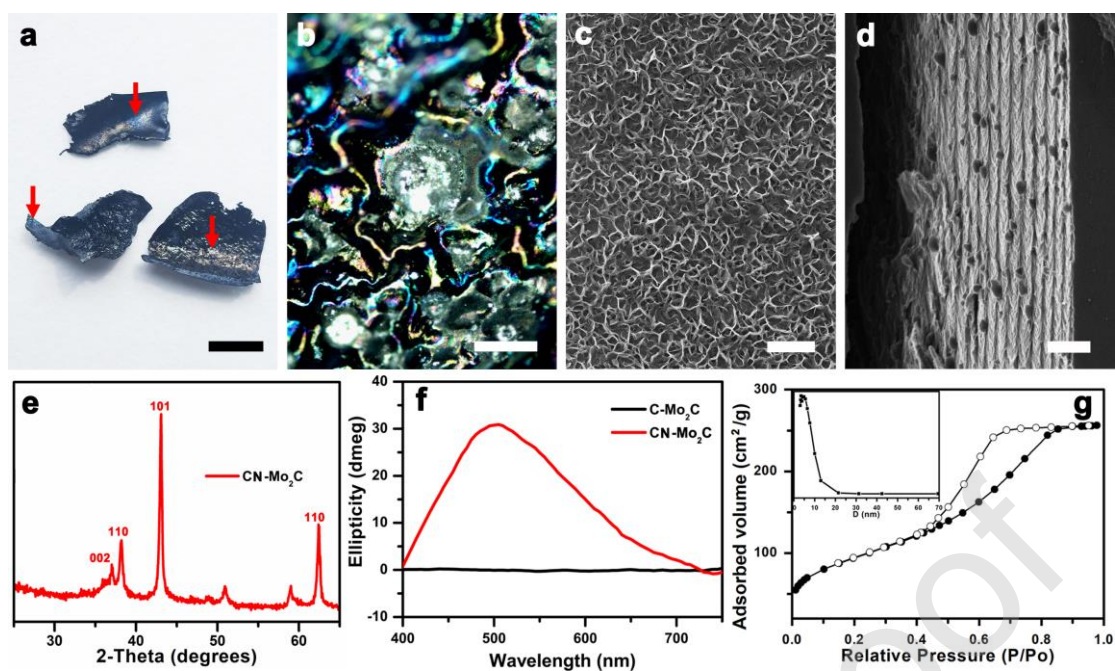


Fig. 3. Freestanding CN-Mo₂C films prepared from MoO₃/C film. (a) Photos of iridescent CN-Mo₂C films (scale bar, 1 cm) and (b) POM image of CN-Mo₂C film (scale bar, 100 μm). (c, d) SEM images of the surface and fracture cross-section of CN-Mo₂C film (scale bar, 500 nm). (e) XRD patterns of CN-Mo₂C. (f) CD signal showing the CN-Mo₂C (red) of the positive absorption, and commercial Mo₂C (C-Mo₂C, black) no absorption band. (g) Nitrogen adsorption-desorption isotherms of CN-Mo₂C films and inset of a BJH pore size distribution.

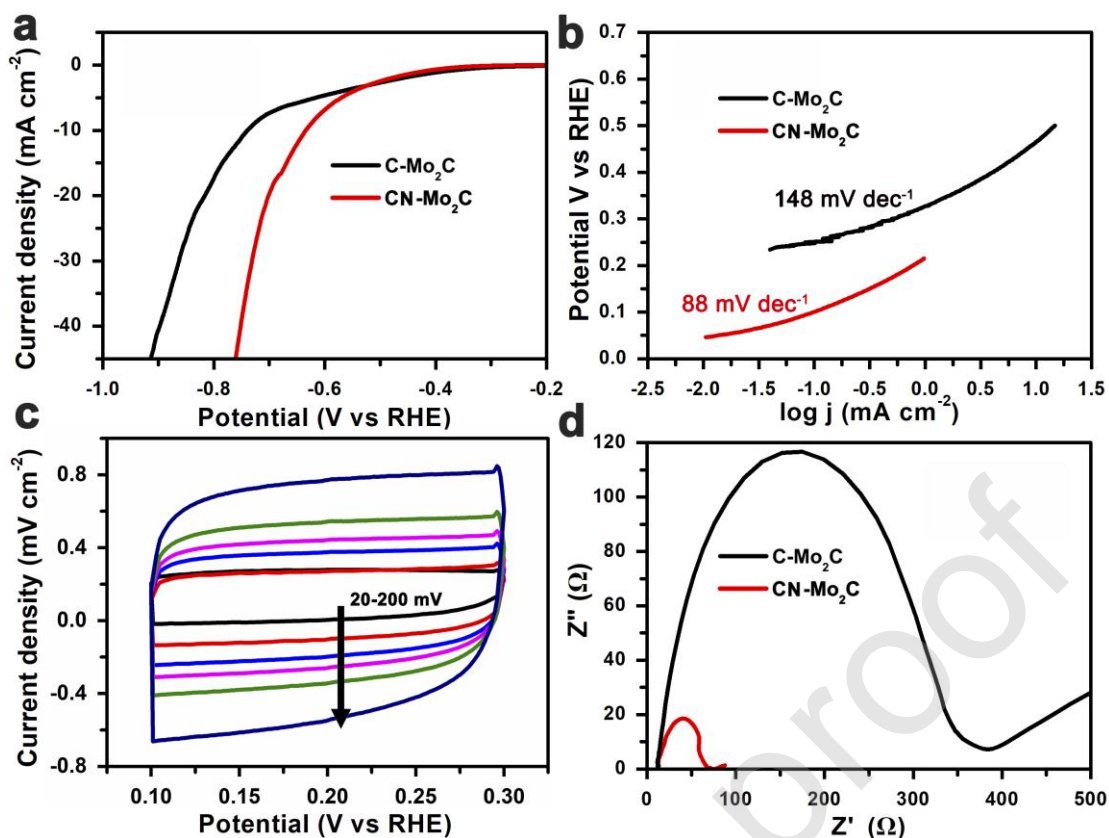


Fig. 4. (a) Polarization curves and (b) Tafel plots of CN-Mo₂C and commercial Mo₂C catalysts. (c) CVs curves of CN-Mo₂C at various scan rates between 20 and 200 mV s⁻¹. (d) Nyquist plots of CN-Mo₂C and commercial Mo₂C at an overpotential of -400 mV.